Efficient photodegradation of methylene blue by CdS-based nanocomposites

S. Fakhri-Mirzanagh[1], S. H. R. Shojaei[1,*], G. R. Pirgholi-Givi[2], and Y. Azizian-Kalandaragh[3,4,5,*]

[1] *Department of Physics, Faculty of Science, Sahand University of Technology, 51335-1996 Tabriz, Iran*

[2] *Department of Advanced Technologies, University of Mohaghegh Ardabili, Namin, Islamic Republic of Iran*

[3] *Department of Physics, University of Mohaghegh Ardabili, P.O. Box.179, Ardabil, Iran*

[4] *Photonics Application and Research Center, Gazi University, 06500 Ankara, Türkiye*

[5] *Photonics Department, Applied Science Faculty, Gazi University, 06500 Ankara, Türkiye*

ABSTRACT

In this research, CdS-based nanocomposites including Ag_2S-CdS, MnS-CdS, and ZnS-CdS were synthesized using the low-cost hydrothermal method for photocatalytic applications. The structural, morphological, porosity, and optical properties of these nanocomposites were examined by X-ray diffraction (XRD), Dynamic light scattering (DLS), Field Emission Scanning Electron Microscope (FE-SEM), Transmission electron microscopy (TEM), Brunauer–Emmett–Teller (BET) method, Mott–Schottky, and UV–Visible spectra. Results proved that nanocomposites prepared at the nanoscale are not so pros. Also, DLS results showed the agglomeration of the particles. The UV–visible results indicated that the band gap of CdS (2.51 eV) changes in the range of 2.15–3.22 eV by adding the transition metal and a suitable amount of impurity metal decreases the band gap of CdS-based nanocomposites. FE-SEM and TEM analyses illustrated that the product was synthesized without impurity at the nanoscale. Position of conduction (CB) and valence band (VB) edges measured by Mott–Schottky analysis, which includes the reduction potential O_2/O_2^- and oxidation potential of $\cdot OH/OH^-$. All in all, ZnS-CdS was the most efficient examined nanocomposite, indicating the best degradation rate of methylene blue (MB) under sunlight due to a small band gap, and appropriate positions of CB and VB.

1 Introduction

Environmental pollution, especially water pollution, is a threat to the creatures' survival and natural environment, and it has become a significant threat to ecosystems and human health, resulting in severe environmental and socio-economic challenges. So, water purification systems have attracted researchers' attention all over the world [1]. Effluents are discharged from various industries, such as textile, paper, rubber, battery, pharmaceutical, and food industries. Moreover, domestic and agricultural wastewater is discharged into natural water sources, directly or indirectly. These pollutants contain organic molecules,

Ⓢ Springer

such as dyes, pesticides, drugs, and aromatic compounds, as well as inorganic molecules such as heavy metal ions that are not decomposed easily [2–4] and have created significant troubles for the natural environment due to their toxicity and abundance.

To address these challenges, several methods, such as adsorption, reverse osmosis, membrane treatment, electrolysis, ion exchange, and photocatalysis, have been explored for the treatment of contaminated water. However, many of these methods either lack optimal operational conditions, are cost-prohibitive, or generate harmful secondary products. Among those, photocatalysis is an efficient, economical, and environmentally friendly method for water treatment, which uses renewable sources and semiconductor materials, while it does not suffer from the aforementioned disadvantages [5].

Photocatalysis is an oxidation process to degrade toxic and organic matter from wastewater without producing secondary toxic materials. This process is carried out under natural/artificial light irradiation of a semiconductor known as the photocatalyst, which plays an important role in the degradation of toxic substances in water. The band gap of a semiconductor is the most effective parameter in a photocatalytic process [6]. Any increase in the band gap of the semiconductor will decrease light absorption and photocatalytic activity [7].

Due to the tunability of their band gap, binary and trinary nanocomposite photocatalysts are considered the best compounds to treat effluents. To improve the photocatalytic activity, the electron–hole recombination must be retarded, and this is possible by using nanocomposites. By introducing a metal into the structure of a semiconductor, the physical and chemical properties of the metal/semiconductor binary nanocomposite completely change. These changes are required to prepare the metal/semiconductor nanocomposite for industrial and optical uses [8]. To absorb a photon, its energy must be equal to or greater than the band gap of the photocatalyst. In this case, the produced charge carriers (electrons and holes) may participate in reduction and oxidation reactions to degrade the trapped toxins on the photocatalyst surface [9, 10].

Several semiconductor materials, such as TiO_2 [11], ZnO [12], MgO [13], SnO_2 [14], CdS [15], and ZnS [16], are potential candidates for photocatalytic applications under visible and UV light. Among these materials, CdS nanoparticles with a 2.4 eV band gap have been widely used [17]. The activity of this nanoparticle is a function of different factors, e.g., phase composition, specific surface area, crystallite size, energy gap, and morphology. CdS has hexagonal and cubic structures. Under a specific thermal treatment, the cubic phase can irreversibly convert into a hexagonal phase [18]. CdS nanoparticles have been investigated in several studies, and it is proven that the degradation is much higher in the nanoparticles synthesized with the solvothermal method [19]. By substituting the solvent with water, the efficiency does not change that much in the hydrothermal method. Therefore, the low-cost hydrothermal method is an efficient and common technique for synthesizing nanoparticles and nanocomposites [20]. Based on extensive research conducted on CdS, it has been demonstrated that even minor modifications in the preparation method and the amount of impurities incorporated into its structure can lead to significant alterations in its optical and structural properties. Recent studies have demonstrated that the band gap of this material is not only affected by different synthesis methods but also varies with changes in temperature during a particular synthesis process. Furthermore, the incorporation of impurities, such as zinc and Cu, and the preparation of ZnCdS nanocomposites with varying ratios of cadmium and zinc ions lead to a significant change in the band gap. Consequently, these modifications impact the photocatalytic activity of the materials, with the degradation rate of methylene blue being notably influenced by the zinc content [21–24].

Cadmium sulfide is one of the best materials in this field due to its suitable potential thermodynamic conditions for photocatalytic redox reactions [25, 26]. Despite the significant photocatalytic advantages of CdS, its high photo-corrosion rate is considered a major disadvantage. This effect is a direct result of the self-oxidation of photogenerated holes [27]. Due to the high rate of electron–hole recombination in CdS, photocatalysis decreases. One of the ways to decrease the recombination rate is to combine CdS with other semiconductors [28, 29]. CdS nanoparticles have a band potential/energy position and good adsorption in the visible region, so they are suitable for photocatalysis, and their photodegradation may be better by adding ZnS [30, 31]. ZnS is known as an effective material in photocatalysis with a wide band gap (about 3.5 eV) because electron–hole pairs are generated quickly, and the excited electrons have large negative redox potentials [32]. When ZnS is added, hydrogen evolution increases depending on the amount of ZnS. Many researchers have obtained these results. In fact, ZnS eliminates the inactive surface

states. The occlusion of these states by Zn^{2+} ions that are in close contact with CdS is possible. Moreover, this may be related to the shift of the conduction band (CB) to a negative position by adding ZnS in an optimized amount. The CB position of ZnS is more negative than that of CdS, which enhances the difference between E_{CB} and $E(H_2/H^+)$ [33–35]. Also, Silver sulfide is an n-type semiconductor that has a narrow band gap of about 0.9–1.0 eV, so the investigation of the optical properties of this semiconductor is attractive. Due to the high rate of electron–hole recombination, the photodegradation of this semiconductor is low. In 2019, CdS-Ag_2S nanocomposites were prepared, and the degradation of methylene orange was investigated. The degradation rate was reported 93.0% in 25 min using visible light irradiation, which is five times higher than that of pure CdS [29], In this case, diffuse bound generated by Ag + ions and cadmium sulfide nanoparticles, and by increasing the amount of silver, the gap be smaller and the takes on the nature of silver sulfide [36].

Based on the promising degradation efficiency of Ag_2S-CdS and MnS-CdS under visible light [37, 38], MnS, Ag_2S, and ZnS were selected as impurity materials in this study. Previous research has primarily focused on incorporating a single metal or semiconductor into the CdS structure, with variations limited to impurity concentration, followed by photocatalytic performance evaluations. However, this study takes a different approach by systematically modifying both the type and concentration of impurities within the CdS structure. The effects of silver sulfide (Ag_2S), manganese sulfide (MnS), and zinc sulfide (ZnS) on photocatalytic activity have been thoroughly examined. Unlike previous studies that investigated only one type of impurity, this work provides a comparative analysis of multiple impurity materials and their impact on CdS photocatalysis. Additionally, the structural and optical differences among the various compositions have been carefully analyzed. These findings offer valuable insights for optimizing the photocatalytic performance of CdS-based materials.

2 Experimental procedures

2.1 Materials

Cadmium nitrate ($Cd(NO_3)_2.4H_2O$), sodium sulfide ($Na_2S.XH_2O$), silver nitrate ($Ag(NO_3)$), manganese nitrate $(Mn)NO_3(_2.4H_2O)$ and zinc nitrate ($Zn(NO_3)_2.4H_2O$) were supplied from Merck company, and in all stages, water was used as the washing agent and liquid solvent.

2.2 Characterizations

All samples were prepared by an ultrasound device (Japan Nasir-Iran). For XRD analysis, a Philips X pert instrument with Cu Kα radiation (λ = 1.5406 Å) was utilized. For the investigation of absorption spectra, a UV-1800 Shimatzu device was used. A MIRA3 FEG-SEM was used to study the effects of morphology and size. To measure the porosity, pore size, and specific area of the samples, BET analysis was done by an II BELSORP mini device (Japan). In the final part, for the calculation of the VB and CB edges of nanocomposites, the Mott-Schottky method was used. This method presents a powerful tool for studying the surfaces of semiconductor electrodes by measuring the flat band. Then, VB and CB edges were obtained from the flat band values.

2.3 Synthesis of nanocomposites

Ag_2S-CdS, ZnS-CdS, MnS-CdS, and pure CdS nano-semiconductors were prepared by a low-cost hydrothermal technique. For the synthesis of the Ag_2S-CdS(1:1)(S1) nanoparticles, 0.1 M solutions of $Cd(NO_3)_2.4H_2O$ and 0.1 M solutions of $AgNO_3$ were prepared in 40 ml of deionized water. Next, these two solutions were mixed for 30 min in a magnetic stirrer. Then, the prepared solution was subjected to 50 W ultrasound irradiation for 30 min. In the next step, 0.1 M Na_2S was added to the above suspension drop by drop. Subsequently, the solution was put in an autoclave at 180 ℃ for 24 h, and then, it was gradually cooled to room temperature. The product was washed five times with deionized water in a centrifuge and dried in an oven at 48 °C. For the synthesis of Ag_2S-CdS(1/2:1)(S2), 0.1 M of $Cd(NO_3)_2.4H_2O$ and 0.05 M of $AgNO_3$ were prepared in 40 ml of deionized water; the stirrer time for all samples was 30 min, and the above steps were repeated. In the same manner, MnS-CdS(1:1)(S3), MnS-CdS(1/2:1)(S4), ZnS-CdS(1:1)(S5), and ZnS-CdS(1/2:1)(S6) were prepared. Pure CdS(S0) was synthesized to compare the results. Table 1 shows the symbols of the samples, and Fig. 1 displays the schematic of the preparation method.

2.4 Photocatalytic activity

The photodegradation properties of the prepared nanocomposites were measured in wastewater using a heterogeneous photocatalysis technique. MB was utilized to test the photocatalytic efficiency of the nanocomposites. The photocatalytic reaction was done under sunlight, and a mercury vapor lamp was used as the UV light source (250 W, $\lambda = 250$ nm). The reactor includes a Pyrex glass beaker, a magnetic stirring device, and a lamp that is positioned above the beaker. In every experiment, 10 mg of dye was dissolved in 1 L of distilled water, and 0.1 g of the produced nanomaterial was dispersed in 100 ml of

this solution by an ultrasonic bath. Then, the prepared solution was placed under a magnetic stirrer in the dark for 30 min to ensure proper homogeneity of the admixture to reach the adsorption equilibrium. After the above steps, the absorption spectra of the prepared solution were measured by using a UV–Visible Shimadzu 1800 device. The photocatalytic process for MB was carried out in two stages. In the first stage, the MB solution was exposed to sunlight, and the amount of degradation was measured every half hour. In the second stage, a UV lamp (250 W, $\lambda = 250$ nm) was used as the light source. In this stage, the temperature was set at 25 °C by a temperature control system. At each step, 4 ml of the solution was taken out of the light source and centrifuged. In this way, the prepared nanocomposites were removed, and after measuring the absorption spectra, they were added to the main solution.

Table 1 Symbols of prepared samples

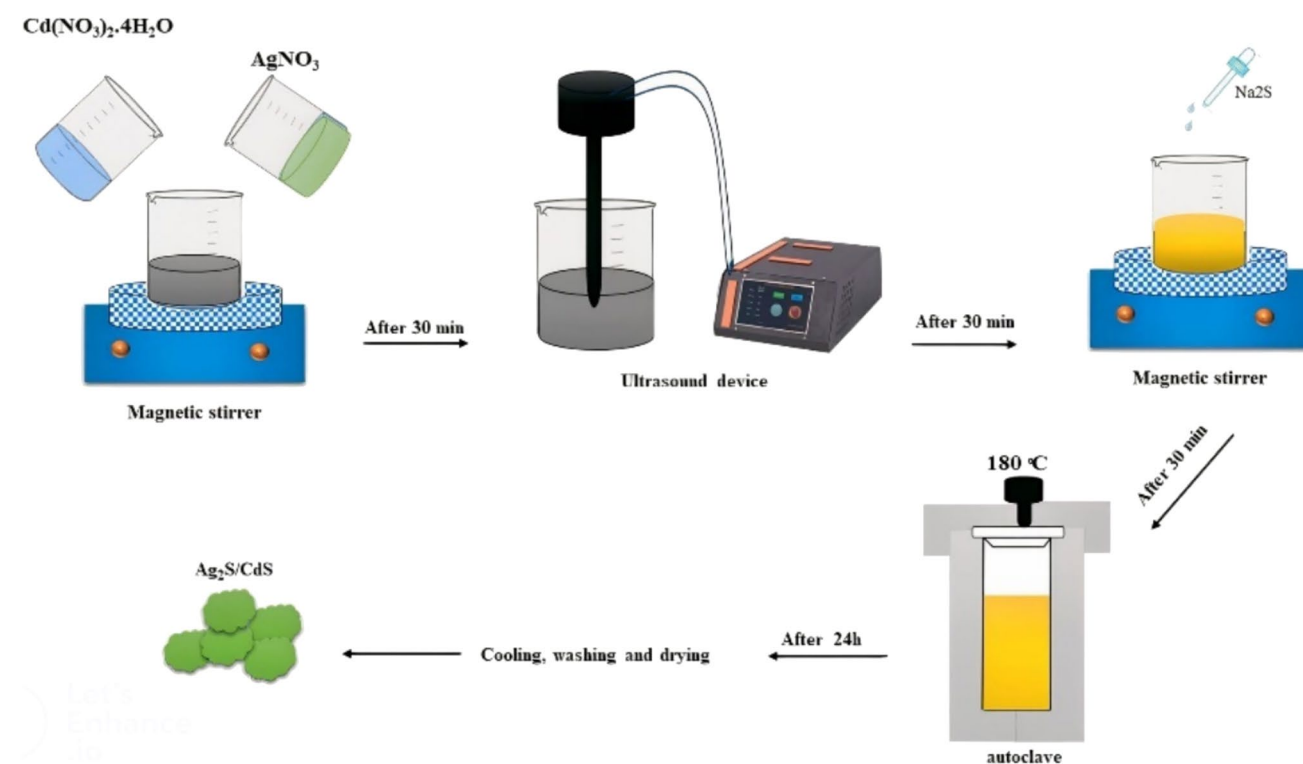| Symbol	Sample
S0	CdS
S1	Ag2S-CdS(1:1)
S2	Ag2S-CdS(1/2:1)
S3	MnS-CdS(1:1)
S4	MnS-CdS(1/2:1)
S5	ZnS-CdS(1:1)
S6	ZnS-CdS(1/2:1)

Fig. 1 Schematic of the preparation method

3 Results and discussions

3.1 XRD analysis

The structural properties of all seven samples that had been synthesized by the hydrothermal method were studied using X-ray diffraction (XRD) over the range of $2\theta = 20 - 80^{\circ}$, and the results are shown in Fig. 2. Seven famous peaks were seen for CdS(S0) in good agreement with the 96–901–1664 reference code (COD database code: 9,011,663). S0 was crystallized in a hexagonal phase with a P63 mc space group, and the lattice parameters (a, b, and c) were obtained to be 4.13, 4.13, and 6.71 angstroms. The results of peaks and the Miler index are given in Table 2. In S1 and S2, the Ag_2S monoclinic phase of nanoparticles was observed (COD database code: 9,011,414) with the Ag_2S peaks seen in the XRD pattern of S1. Therefore, CdS-Ag_2S nanocomposites were prepared by the hydrothermal method. In S3 and S4, MnS with a cubic phase is introduced into the CdS structure. The MnS peaks can be observed (JCPDS 40–1289) in Fig. 2. Moreover, in S5 and S6 samples, the hexagonal peaks of ZnS can be seen (COD database code: 9,013,420). Accordingly, CdS-Ag_2S, CdS-MnS, and CdS-ZnS nanocomposites were synthesized. Table 2 shows all Miler indices and space groups of the prepared nanocomposites.

The size of nanoparticles is an important parameter in their properties. Therefore, the size of the prepared nanocomposites was calculated from XRD results. There is a very effective method in this field based on the Debye–Scherrer and Williamson-Hall relations, which was used in this work. The Debye–Scherrer equation is expressed as follows [39]:

$$D = \frac{0.9\lambda}{\beta \cos\theta} \tag{1}$$

In the Scherrer method, it is assumed that just the width of diffraction pattern peaks plays an important role in the size of the crystals, so other factors are not considered. A crystal lattice defect is one of these factors that arises from the presence of impurities, lattice displacement, etc. Since these factors cause stress and strain on the crystal lattice, they affect the width and intensity of Bragg peaks. Using the Williamson-Hall relation, not only can the size of particles be calculated, but also the amount of stress on the crystal structure can be obtained as follows [40]:

$$\beta \cos(\theta) = \varepsilon \times \sin(\theta) + \frac{k\lambda}{D} \tag{2}$$

In Eqs. 1 and 2, D, λ, ε, β, and θ are the size of nanostructures, the width of a peak, strain, X-ray wavelength, and diffraction angle, respectively. Table 3 illustrates the size of nanostructures using two methods (values are approximated and written after averaging. The obtained values show the difference between the two methods well. The values obtained from the Williamson-Hall method are larger than those obtained from the Debye–Scherrer method. Both methods make simplifying assumptions, so the calculated amounts are different from reality.
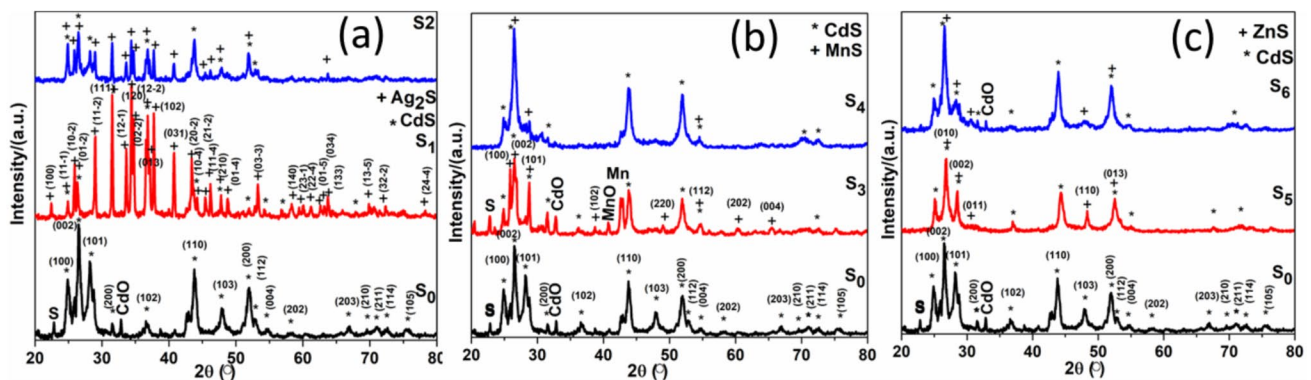

Fig. 2 XRD spectra of samples, **a** S0, S1, and S2, **b** S0, S3, and S4, **c** S0, S5, and S6

Table 2 XRD analysis results for prepared nanocomposites

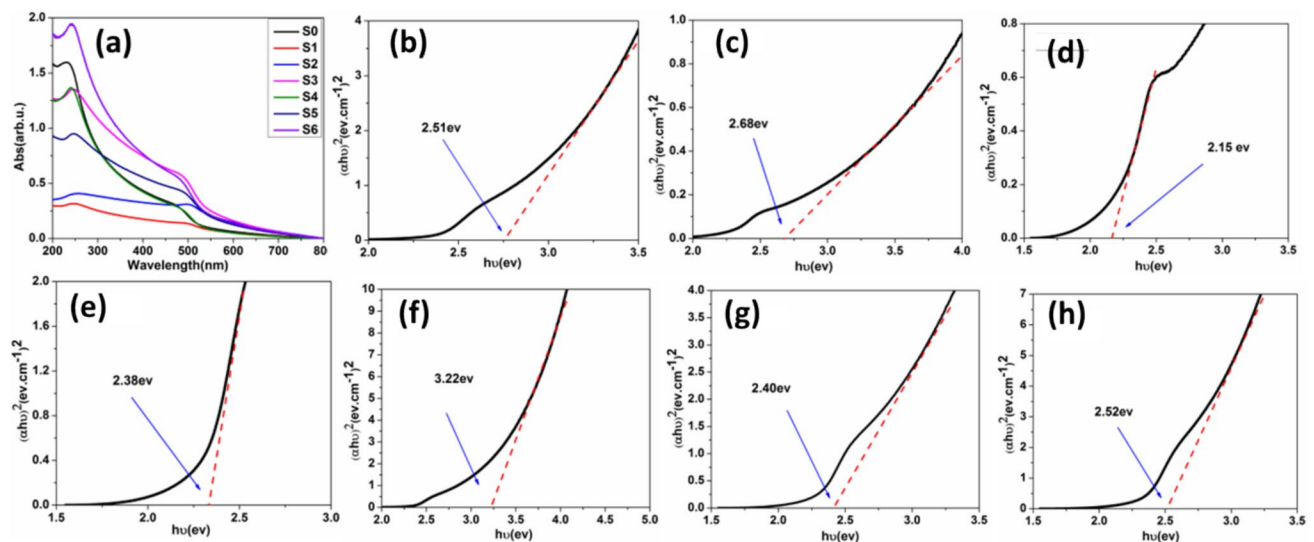| Sample	2θ(degree)	Miller index	Space group	Phase	a, b, c(Å)
S$_0$[41]	24.8, 26.5, 28.1, 31.5, 36.6, 43.7, 47.9, 51.3, 51.9, 52.9, 54.9, 58.1, 66.9, 69.8, 71.1, 72.6, 75.5	(1 0 0), (0 0 2), (1 0 1),(2 0 0), (1 0 2), (1 1 0), (10 3),(200), (1 1 2),(201),(004),(202),(203), (210),(211),(114),(105)	P63 mc	Hexagonal	4.13 4.13 6.71
S$_1$, S$_2$[42]	22.4, 24.9, 25.8, 26.3, 28.9, 31.5, 33.6, 34.4, 34.7, 36.8, 37.0, 37.7, 40.7, 43.3, 44.1, 45.3, 46.1, 47.7, 48.7, 53.2, 58.2, 59.4, 59.9, 61.2, 62.5, 63.7, 69.8, 72.3, 78,3	(1 0 0),(1 1 −1) (1 0−2),(0 1−2),(1 1–2), (1 1 1), (1 2 −1), (1 2 0),(0 2−2),(1 2−2), (0 1 3),(1 0 2), (031),(2 0−2), (1 0–4), (2 1 0), (0 1−4),(0 3 −3), (1 4 0), 0–4), (2 1−2), (1 1 −4), (2 1 0), (0 1−5), (0 3 4), (1 3 −5),(3 2 −2), (2 4 −4)	P121/c1	Monoclinic	4.23 6.91 8.29
S$_3$, S$_4$[43–45]	25.6, 27.0, 28.9, 38.6, 49.0, 54.7, 60.6, 65.5,	(1 0 0), (0 0 2) (1 0 1), (1 0 2), (2 2 0) (1 1 2), (2 0 2), (0 0 4)	Fm −3 m	Cubic	4.95 4.95 4.95
S$_5$, S$_6$[46]	26.5, 28.1, 30.5, 48.3, 52.5	(0 1 0), (0 0 2), (0 1 1), (1 1 0) (0 1 3)	P63 mc	Hexagonal	3.8 3.8 6.2

3.2 Absorbance

To investigate the optical properties of the prepared samples, the absorption spectra of these nanomaterials were measured, and the results are demonstrated in Figure 3. The main peak of S0 is seen at 232.50 nm, and for S1, S2, S3, S4, S5, and S6 is obtained at 249.50, 256.58, 246, 241.5, 248.48, and 244.01 nm, respectively. The first peak is the absorption spectrum of the samples, and the others are related to the bandgap of the samples. The optical, electrical, magnetic, and physical properties of nano-semiconductors strongly depend on the morphology, size, structure, and band gap of the samples. Consequently, one of the methods for measuring the band gap of nanomaterials is explained by using the absorption spectrum. In this method, the optical absorption coefficient α is calculated by the following formula [47]:

$$\alpha h\upsilon = B\left(h\upsilon - E_g\right)^n \tag{3}$$

where $h\upsilon$ is the energy of the photon, B is a constant, and n = 0.5 for a direct band gap. By plotting $(\alpha h\upsilon)^2$ against $h\upsilon$, the band gap of nanomaterials can be obtained. In this way, the band gap of CdS is obtained to be 2.51 eV. Research has proven that by adding a suitable amount of silver to cadmium sulfide, the band gap decreases [29, 48]. Therefore, the band gaps of S1 and S2 were calculated to be 2.68 and 2.15 eV. Additionally, it is demonstrated that the intensity of CdS absorption spectra increases with the addition of Zn, and the band gap decreases [49]. The band gap of S5 was obtained as 2.40 eV, which is smaller than that of S0. Some results indicate that, at small wavelengths, absorption increases by decreasing the Mn amount in samples, leading to a large band gap; S4 has a band gap of about 3.22 eV [50]. Table 3 shows the values of the band gap for all samples. By adding transition metals, the band gap is changed. The electronic band structure of materials plays an important role in the realization of photocatalytic properties of semiconductors. When the irradiation of light gives an energy higher than the bandgap, the electrons of VB are excited to CB. Therefore, the excited electrons turn on the hydrogen evolution reaction. The bandgap is an intrinsic value that depends on the structure of the composition. This factor is a basic characteristic of photocatalytic processes [51, 52]. Semiconductors with large band gaps need more energy to separate the charge carriers and start the photocatalytic process. As

Table 3 Obtaining particle size from XRD, bandgap from Abs, grain size, and atomic percent from FESEM for a11 7 samples

Sample	Debye–Scherer D(nm)	Williamson–Hall		Bandgap(ev)	Grain size(nm)	Element percent	
		D(nm)	ε			Elt	A%
S0	18	41	3.5×10^{-3}	2.51	39	S	52.80
						Cd	47.20
S1	13	14	10×10^{-3}	2.68	40	S	42.47
						Ag	38.90
						Cd	18.63
S2	16	36	4×10^{-3}	2.15	38	S	46.79
						Ag	18.51
						Cd	34.70
S3	15	17	8.3×10^{-3}	2.38	37	S	49.87
						Mn	0.84
						Cd	49.29
S4	24	50	2.9×10^{-3}	3.22	38	S	48.34
						Mn	0.37
						Cd	51.29
S5	25	90	1.6×10^{-3}	2.40	45	S	44.54
						Zn	16.73
						Cd	38.72
S6	20	33	4.3×10^{-3}	2.52	50	S	50.11
						Zn	5.39
						Cd	44.50

Fig. 3 UV–Visible Spectroscopy, **a** absorption spectrum and **b** Variation of $(\alpha h\nu)^2$ with $h\nu$ for S0, **c** S1, **d** S2, **e** S3, **f** S4, **g** S5 and **h** S6

a result, the small band gap is considered the first factor at the beginning of the process. For S5, S2, and S3, the decrease in the gap can be seen in Fig. 3.

3.3 SEM and EDX

The surface morphology and size of the prepared nanocomposites were studied by FESEM analysis.
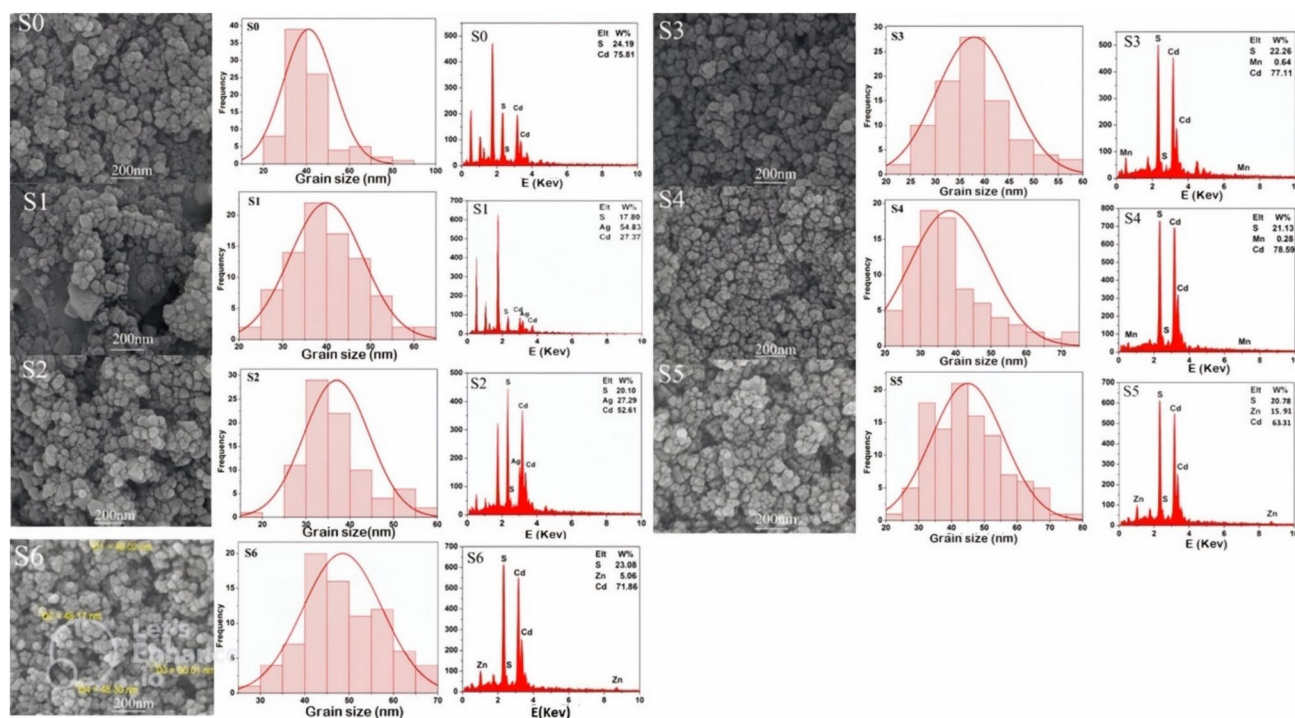
Fig. 4 SEM image and EDS analysis of CdS-based materials

The surface of the samples was photographed using a scanning electron microscope (SEM). The results for all samples are illustrated in Fig. 4 in the form of sphere-like nanometer-sized particles. All samples had the same structure with similar grain size. The grain size of the samples was obtained to be about 50 nm, and these spherical particles were non-uniformly adhered. Figure 4 shows the size distribution of all samples obtained from SEM analysis. The average size of CdS(S0) was measured to be about 39 nm; for other samples, this parameter was 40, 38, 37, 38, 45, and 50 nm, respectively, Moreover, to investigate the stoichiometric properties and purity of the nanomaterials, the elemental characterization of X-ray energy diffraction spectroscopy (EDX) was used. The obtained results indicate the presence of Ag, Mn, and Zn metals in the structures, and by decreasing the ratio of these metals to cadmium, their percentage in the produced structures was reduced. It is a normal and predictable result for the S1 sample because silver has higher reactivity than cadmium and is deposited faster in the structure. Table 3 demonstrates the grain size and elemental percentage of all samples.

3.4 TEM

TEM is an analytical technique that is useful for the investigation of the smallest structures of particles. Figure 5 displays the TEM image of the prepared nanocomposites. The results represent a homogeneous distribution in which the morphology of nanocomposites changes by changing the impurity. The Size distribution histogram of samples plotted in Figure 5, for S0, grain size ranged from 6 to 12 nm. In Figure 5b, Ag_2S nanoparticles caused to aggregation enhancement with a size range of 15–20 nm; also, the S5 sample size distribution ranged in wider diameters about 7–11 nm. According to TEM images, the nanocomposites are shaped in the spherical form, that have in good agreement with the SEM results.

3.5 DLS

Dynamic light scattering (DLS) analysis was used to investigate and compare the size of prepared nanoparticles by studying the hydrodynamic size distribution. Figure 6 illustrates the size distribution of prepared nanocomposites. As shown in Fig. 6, all samples were
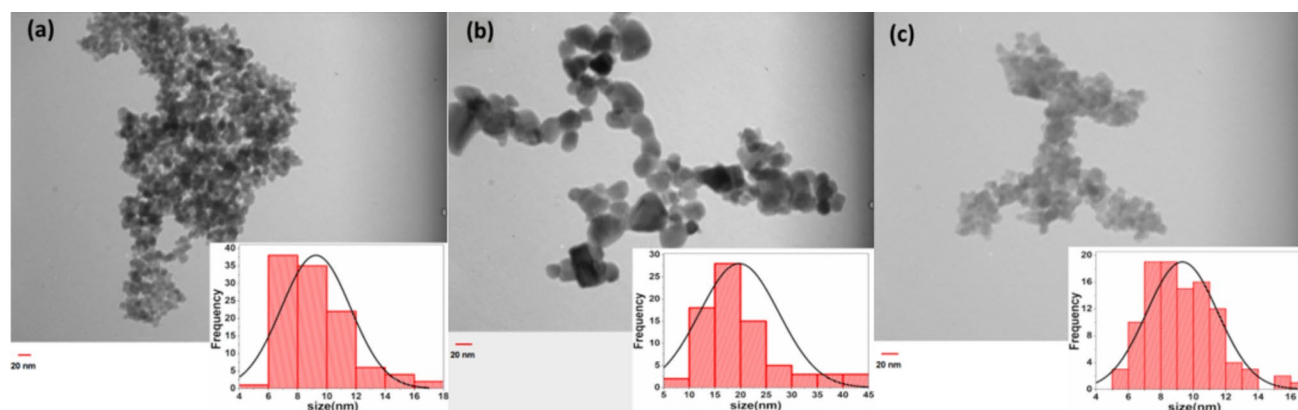
Fig. 5 TEM image of prepared nanocomposites, **a** pure CdS, **b** S2, and **c** S5
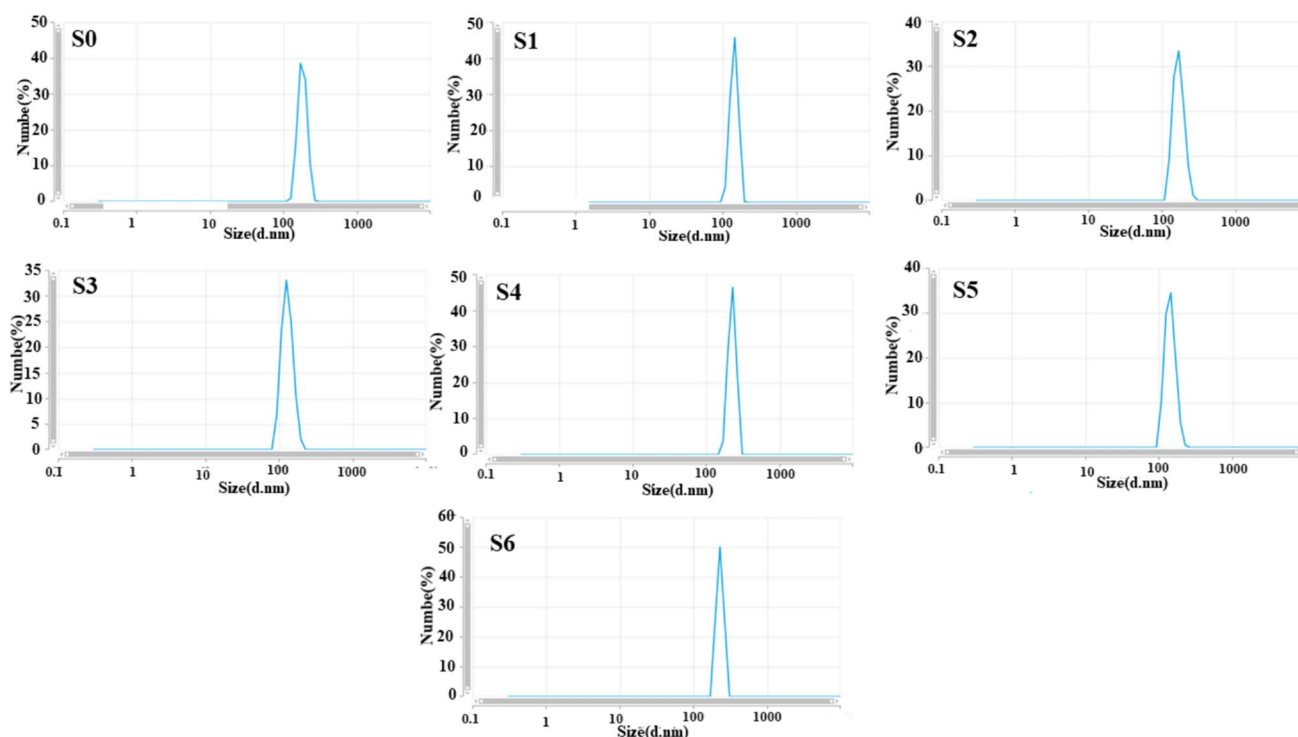

Fig. 6 DLS analysis plot represents the particle size distribution for S0, S1, S2, S3, S4, S5, and S6

synthesized in the same size distribution, and there is no significant difference in as Debye-Scherer and SEM methods. The dynamic light scattering measurements are indicative of nanoparticle diameter. Actually, in bad dispersion, DLS deals with the collected or agglomerated structures as a single molecule and measures their whole size [53, 54]. Thus, nanocomposites with a big size distribution are shown in Fig. 6 and Table 4. In the X-ray diffraction analysis, the X waves diffracted from the surface of polycrystals, and

Table 4 DLS analysis measurement data in size distribution of samples

Sample	Size(d.nm)
S0	169.9
S1	146.1
S2	169.9
S3	125.6
S4	229.8
S5	146.1
S6	229.8

the Debye–Scherrer formula could be used to obtain the average crystallite size. But, in the DLS, light scattered from a bunch of (clusters) crystallites, so, gives the average particle size. It is clear that the average crystallite size is smaller than the average particle size [55].

3.6 BET

For studying the specific surface areas and pore size distributions of the prepared nanocomposites, Brunauer–Emmett–Teller (BET) analysis was carried out. In this method, a specific surface area is obtained in m^2/g. In nanocomposites, by increasing the surface area, the photocatalytic activity increases [56]. This happens because by increasing the surface area, the amount of adsorption active sites on the surface

Table 5 Obtained Surface area, pore size and pore volume of samples from BET analysis

Sample	$a_{s, BET}$ (m^2/g)	Pore size (nm)	Pore volume (cm^3/g)
S0	65.60	8.03	0.226
S1	2.25	21.79	0.079
S2	13.10	1.66	0.052
S3	54.36	10.65	0.228
S4	47.61	7.00	0.208
S5	49.13	12.22	0.229
S6	54.41	8.03	0.224

is enhanced, so the redox reactions are increased by electron–hole pairs [57]. Additionally, decreasing the size of nanoparticles increases the surface area and active sites [58]. Therefore, the BET surface area for CdS(S0) was obtained to be about 65.6 m^2/g, similar to the results of references [59, 60]. The calculated average pore size and pore volume were measured to be about 8.03 nm and 0.226 cm^3/g using the Barrett-Joyner-Halenda (BJH) method. BET analysis results of all samples are presented in Table 5 and Fig. 7. The shape hysteresis loop shows H1 configurations by cylindrical mesopores [61], which is seen in all samples except the Ag blend samples. Four regions exist in the adsorption/desorption curves. The first region is $p/p_o < 0.2$, which is related to the monolayer adsorption of N_2 molecules on the walls of the mesopores. The second region is limited to $p/p_o > 0.25$ and $p/p_o < 0.5$, in which, because of capillary condensation inside the mesopores, absorption increases. In the third region, adsorption occurs in the horizontal direction because of the multilayer adsorption on the outer surface. Finally, in $p/p_o > 0.9$, the increase in absorption is demonstrated by the large pore diameter [62]. Materials with large surface areas are a good choice for photocatalysis because a large surface area increases the adsorption of pollutants, and the degradation time decreases. However, this is not always true, and a large band gap increases the degradation time [63]. Although a large effective surface area increases the photocatalytic activity, this activity decreases with the
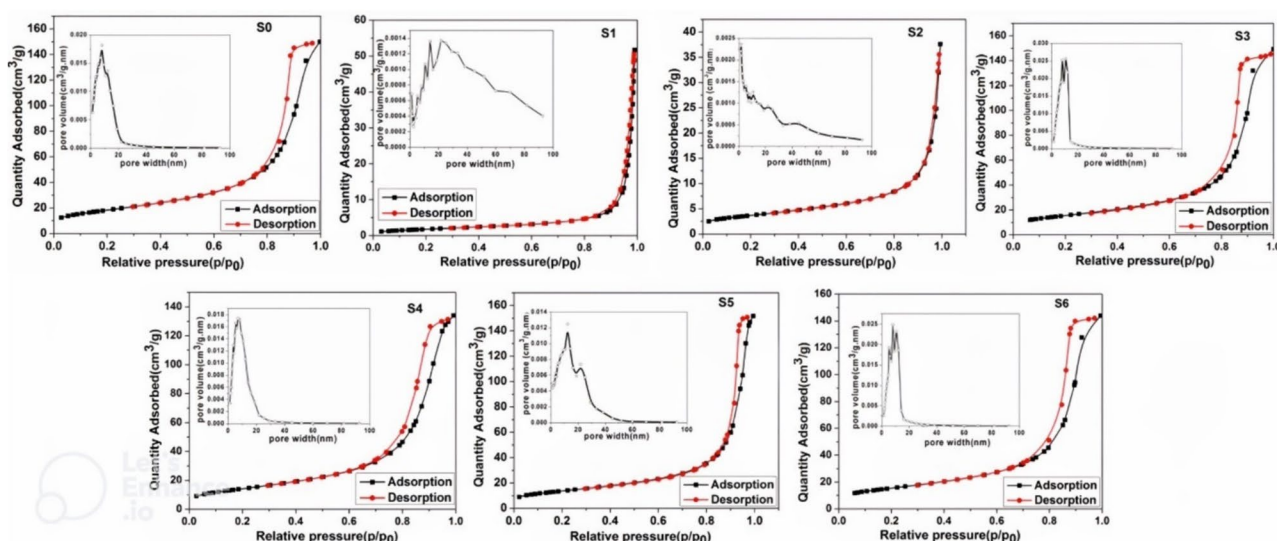

Fig. 7 The BJH pore size distribution diagram, N_2 adsorption and desorption of samples obtained from BET analysis

smaller size of the pores, and the material with a larger pore size is the winner, as happened for S5 [64]. Based on Table 5, the pore size for all samples is in the 2–50 nm range, which is the mesoporous range (according to the classification in reference [65]). The pore size of S3 is 1.66 nm (0.2–2 nm), which is in the microporous range (according to IUPAC classification)[65].

3.7 Mott–Schottky

The Mott-Schottky (MS) plot was used to understand the band edge positions of the prepared materials concerning reversible hydrogen electrode (RHE) values and water-splitting potentials. A positive slope in the linear region of the MS plots can be observed for all cases (Fig. 8). The positive slope indicates the n-type and the negative slope indicates the p-type behavior of the semiconductors. MnS is a p-type semiconductor, so a negative slope is seen in the MS plot of MnS-CdS. The flat band potential values obtained from the MS plots indicate the position of the conduction band edge of semiconductors. Precisely, for n-type semiconductors, the conduction band edge can be positioned at a slightly lower potential concerning the flat band potential. Therefore, the conduction band edge of nanomaterials is expected to be at less than 0.1 V of

the flat band potentials [66, 67]. In Fig. 8, the MS plot of the prepared samples is shown, and the flat band energy is determined. Therefore, the positions of the valence band and conduction band for all samples can be calculated. The conduction and valence band edges are other important parameters to set the hydrogen evolution reactions, and the positions of the edges are useful in many cases. It is proven that the position of conduction band edges must be equal to or more negative than the proton reduction potential (H_2/H^+) in spontaneous reactions. In addition, if the activation energy of reaction pathways is considered larger than the thermodynamic potential, it should be provided to the reaction system. In this condition, the potential gap is referred to as overpotential. Consequently, the suitable selection of semiconductors is restricted to two types. The band gap must be in the visible range with enough overpotential [51]. Moreover, semiconductors whose valence band is more positive than the oxidation potential (H_2O/O_2) must have enough potential for producing oxygen from the water photocatalytic process [68].

Figure 9 shows the diagram of the band positions. It seems that the competition for the degradation of pollutants is among S0, S2, and S5 because they have the lowest bandgap energy. Moreover, the positions

Fig. 8 Plot of the Mott-Schottky of prepared samples by the hydrothermal method
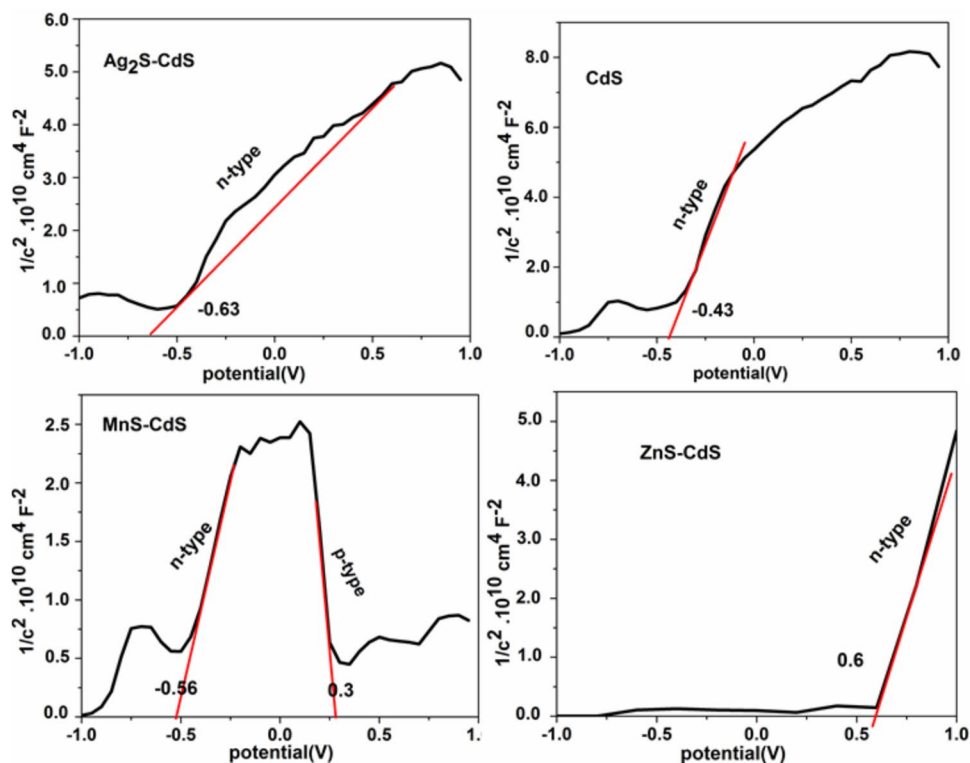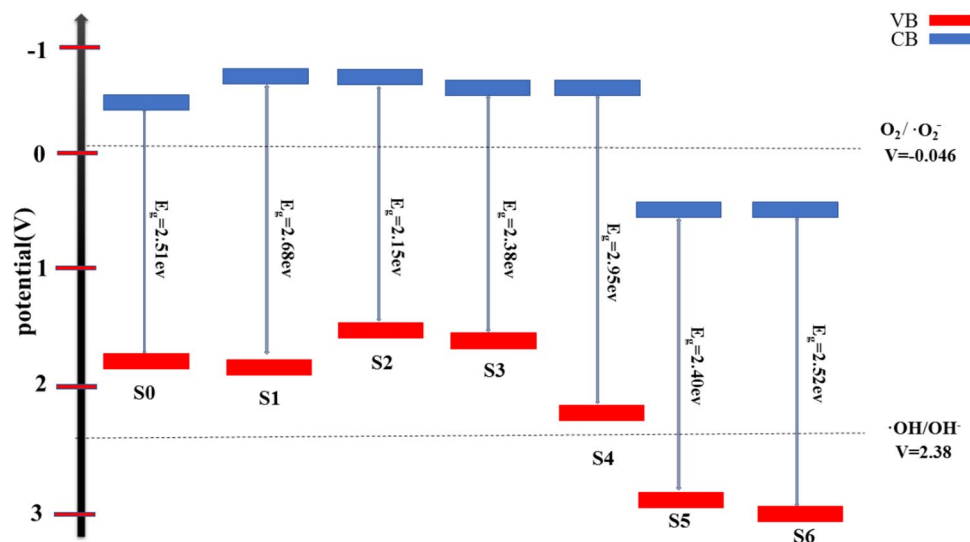
Fig. 9 Diagram of band position and E_g for CdS(S0) and other CdS-based semiconductors

of CB and VB have a crucial effect on pollutant degradation. The position of the CB of ZnS-CdS was lower than the reduction potential of $O_2/^{\cdot}O_2^-$ and the CB of other nanocomposites was higher than this potential. Additionally, the VB of ZnS/CdS was lower than the oxidation potential of $^{\cdot}OH/OH^-$, but the position of the VB of other samples was higher than this potential. Therefore, in ZnS-CdS, holes and hydroxyl radicals were produced in the photocatalytic process, but in other cases, this was not possible, i.e., the photocatalytic activity of other cases had low efficiency [69].

4 Photocatalytic process

In this section, the photocatalytic properties of the materials that were prepared by the hydrothermal method are investigated. There are some important parameters, such as the adsorption of pollutants, charge transportation, light harvesting, and carrier separation, in photocatalytic reactions [7, 70]. MB was selected as an organic pollutant to evaluate the ability of the prepared nanostructures to degrade dye under light sources. Photodegradation of MB by time, under Sunlight and UV light source, has been plotted in Figs. 10 and 11. The absorption peak
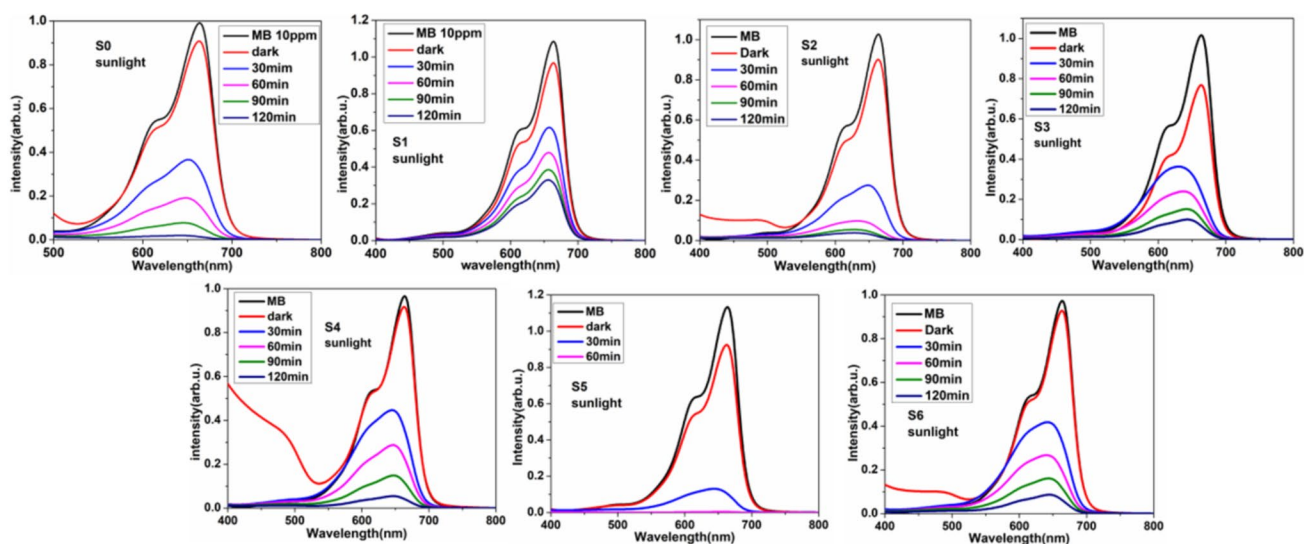

Fig. 10 Absorption spectra of MB degradation under sunlight irradiation by CdS-based nanocomposites
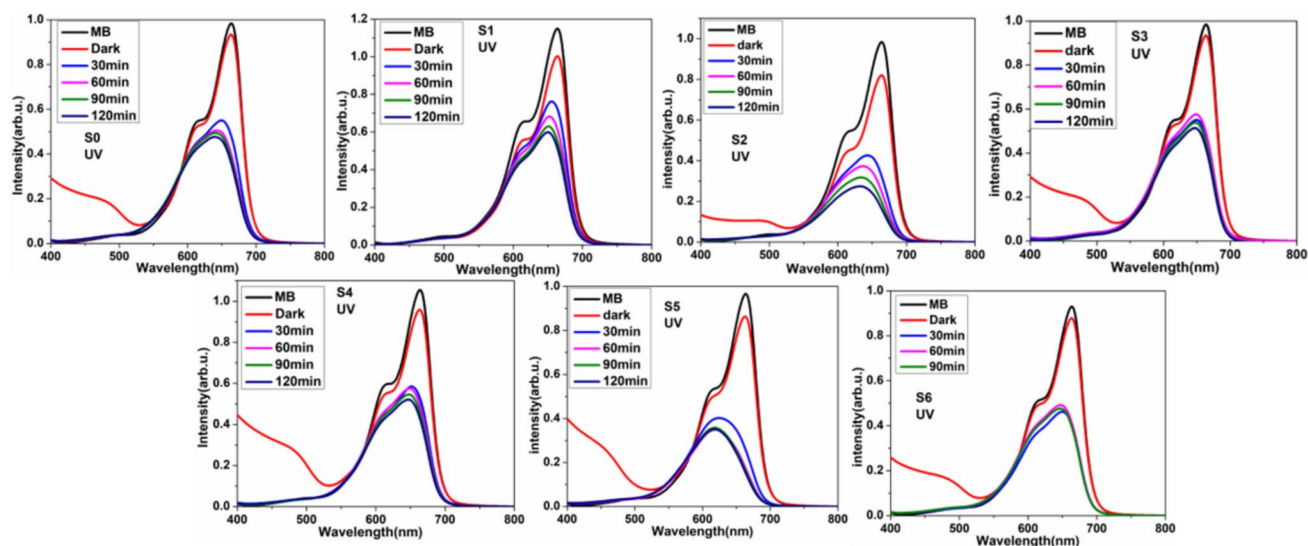
Fig. 11 Absorption spectra of MB degradation under UV irradiation by CdS-based nanocomposites

intensity of the MB has decreased by increasing the light irradiation time. S5 under sunlight for 60 min has reduced the intensity of the MB absorption peak to about zero, which means that the pollutant has been completely removed. Samples S0, S2, and S4 have reached over 90% degradation in 120 min under sunlight irradiation. Also, in Fig. 11, as can be seen, the S5 sample has been successful in MB degradation under UV irradiation, although it has not completely reduced the absorption peak intensity, it has performed better than other samples. Sample S2 is ranked second in MB degradation in Fig. 11 again. Other samples have almost the low and same low performance.

Figure 12 demonstrates the degradation percentage of MB under two light sources. Degradation percentage is obtained as follows [71]:

$$Degradation\ Efficiency\% = (\frac{1 - A_t}{A_0}) \times 100 \qquad (4)$$

where A_0 is the initial concentration of the pollutant and A_t is the concentration of the pollutant that remains after degradation. As can be seen, the ratio of metal added to the CdS nanostructure has a significant effect on the degradation process. Based on the results discussed in the previous sections, the above results were predictable. The competition to remove the pollutant is between three samples S0, S2, and S5. Sample S2 with a small bandgap has succeeded in two cases. According to previous studies, the incorporation of silver sulfide into CdS structure enhances the degradation efficiency of MB, with the degradation process being influenced by the pH of the environment[72]. A suitable percentage of Zn improves the photocatalytic

Fig. 12 Photodegradation percent, **a** MB degradation under Sunlight and **b** MB degradation under UV light irradiation
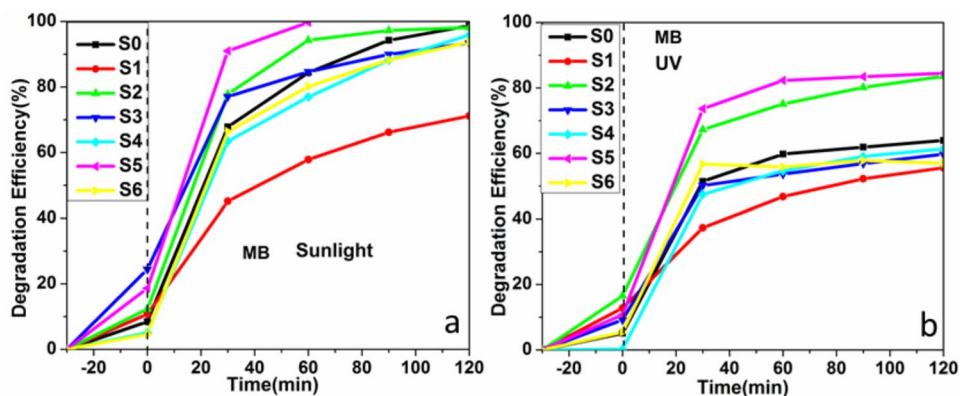
process [73] such that S5 with the 1:1 ratio of Zn and Cd, removes a large amount of MB over 1 h under sunlight. In the UV source, S5 does not reach 100% degradation, but it has the best activity among all the prepared samples, while it reaches 99% degradation under sunlight. This may be due to the high power of sunlight. These results have been predicted by previous analyses. High specific surface area, large pore size, small band gap, and good position of VB and CB are effective factors for this phenomenon.

For a more detailed study of the photocatalytic activity of the prepared materials, the photocatalytic degradation kinetics is expressed by the Langmuir–Hinshelwood mechanism as follows [74]:

$$Ln(\frac{C}{C_0}) = -K_{app}t \tag{5}$$

where C_0 and C are the initial and post-degradation concentrations of the pollutant; K_{app} and t are the degradation rate and time. By plotting $ln(C/C_0)$ versus time, the slope of the curve gives the degradation speed. Figure 13, K_{app} is demonstrated for MB in all samples under two light sources. It can be seen

that S5 has a high degradation speed for MB under sunlight. This was proven in previous sections. Sample S5 has a narrow band gap, includes the reduction potential, and exhibits appropriate positions of CB and VB. These properties make S5 more photoactive than other samples in the degradation of MB dye. Sunlight is more efficient than UV lamps because it covers a wide range of wavelengths. Furthermore, the band gaps of materials are in the visible region, so the degradation of MB by sunlight is successful.

To investigate the capacity of S5 (ZnS-CdS(1:1)), the desorption test was carried out, and these nanoparticles were used for the second and third times for the degradation of MB in water. Recyclability is an important parameter for photocatalyst nanoparticles. Ease of recovery and stability of the photocatalyst are important factors in the efficiency of degradation [75]. Therefore, S5 was initially used to degrade MB in one hour. Next, nano-powders were separated from the solution by centrifuging, and then they were dried and recycled. After this step, the dried nanocomposite was used a second time to degrade the MB solution without adding extra nano-powder. This procedure was carried out for the third time, and the results are shown in Fig. 14. Sample

Fig. 13 The Langmuir–Hinshelwood mechanism for the speed of photocatalyst activity. **a** MB degradation under Sunlight and **b** MB degradation under UV lamp irradiation
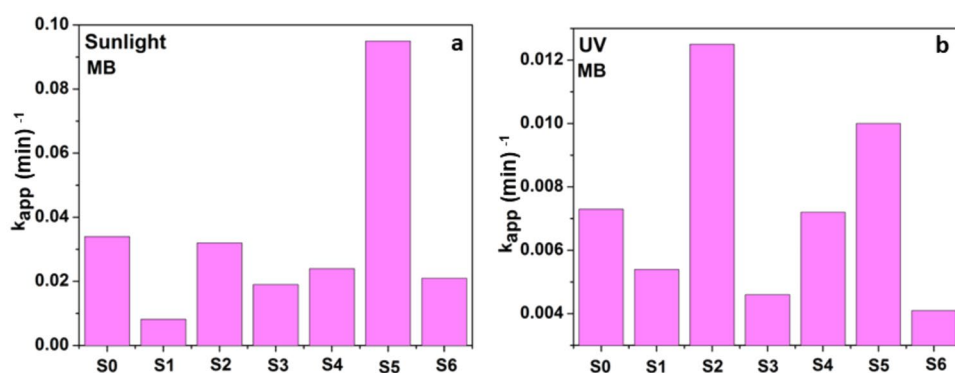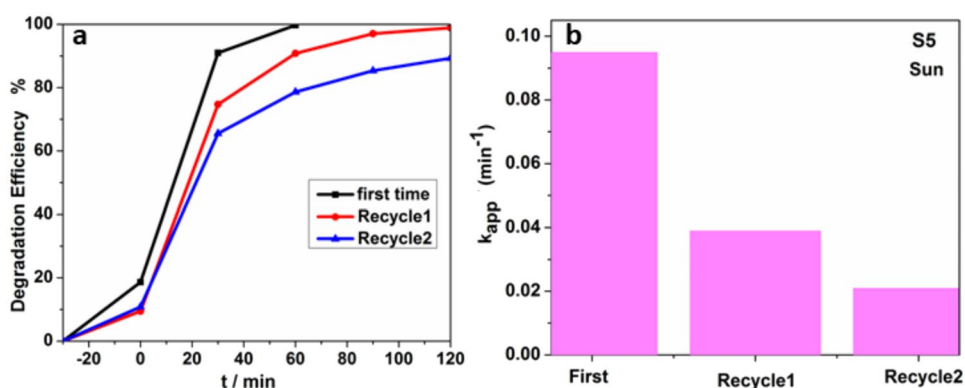

Fig. 14 First, second, and third time MB degradation under the sunlight by S5. **a** degradation percent and **b** kinetics of reaction

S5 could degrade the pollutant completely after 90 min on the second time and after 120 min on the third time. This indicates that desorption does not occur in the prepared semiconductors, so they can be widely used. The Langmuir–Hinshelwood mechanism for recycling S5 is shown in Fig. 14b. It is observed that by increasing the cycle, the efficiency decreases [76]. Structural changes, particle size, location of absorption peaks, changes in surface area, and other properties of nanomaterials after their use in the photocatalytic process are the reasons for the changes in their degradation capacity after several times of recycling [75]. Therefore, the decrease in degradation of S5 after twice recycling can be attributed to the decrease in absorption surface area, increase in band gap, increase in particle size, change in structure, etc.

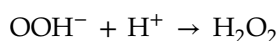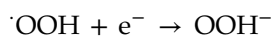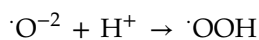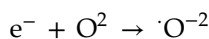The mechanism of pollutant degradation can be written as follows:

Photon energy transfers electrons from the valence band to the conduction band, and electron–hole pairs are generated.

$$Photocatalyst + h\nu \rightarrow e^-_{CB} + h^+_{VB}$$
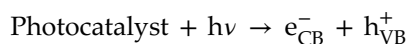
Carriers have an important role in reduction and oxidation reactions, which finally degrade pollutants. Holes react with hydroxyl ions:

$$H_2O + h^+ \rightarrow OH^- + H^+$$

$$h^+ + OH^- \rightarrow {}^\cdot OH$$
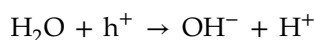
Hydroxyl radical, which is responsible for the degradation of pollutants, is produced. Additionally, electrons in the conduction band react with oxygen in the environment:

$$e^- + O^2 \rightarrow {}^\cdot O^{-2}$$

$${}^\cdot O^{-2} + H^+ \rightarrow {}^\cdot OOH$$

$${}^\cdot OOH + e^- \rightarrow OOH^-$$

$$OOH^- + H^+ \rightarrow H_2O_2$$

Hydrogen peroxide acts as a barrier for preventing electron–hole recombination [5]. The mechanism of degradation of pollutants and corresponding reactions are shown in Fig. 15.

5 Conclusions

In this research, binary semiconductors based on cadmium sulfide were prepared. Transition metals (Mn, Zn, and Ag) were introduced as the second material with different rates to investigate the effect of the type and ratio of the metal on the properties of the prepared nanocomposites. To study the structural, morphological, and optical properties of the samples, XRD, FESEM, TEM, BET, DLS, and UV–Visible analyses were conducted. The results showed that the samples had been synthesized without impurities on

Fig. 15 Mechanism of degradation of pollutants and reactions
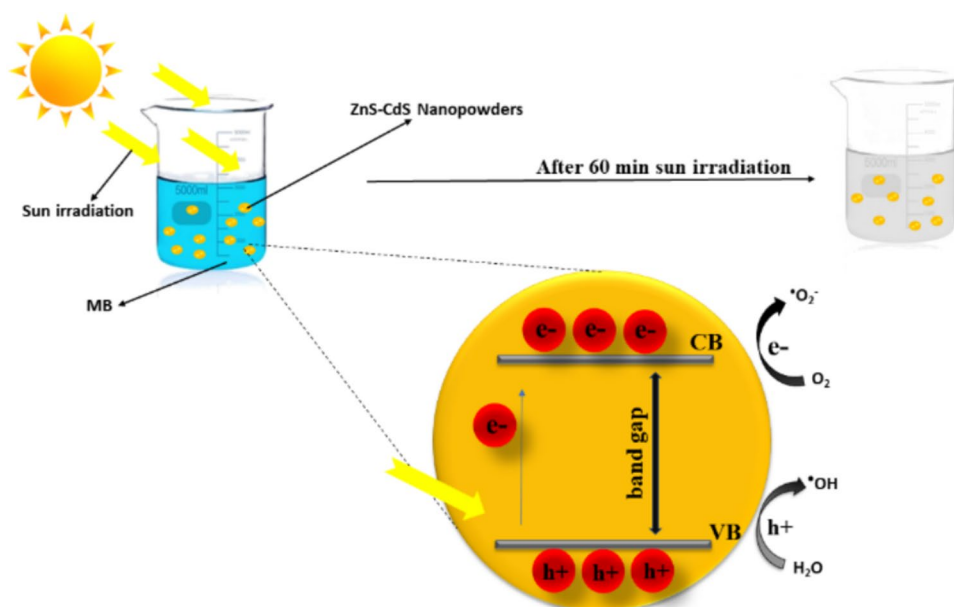
the nanoscale, without significant differences in the size of the materials. The peaks of silver sulfide (Ag_2S), manganese sulfide (MnS), and zinc sulfide (ZnS) were observed in the XRD pattern. In many cases, Mn, Zn, and Ag decrease the band gap of CdS, so they are acceptable for photocatalytic activity (S2 and S5). The large pore size of S5 makes it effective in the degradation of MB, even though it has a small specific area. The valence band edge and conduction band edge energies of S5 are lower than the oxidation and reduction potentials, respectively. Therefore, S5 performs better in the degradation of MB under sunlight and UV. Sample S5 can remove the pollutant from water in an hour at a high rate, and the absorption and desorption test showed that it can be introduced as a recyclable photocatalyst.

Acknowledgements

Author contributions

All authors contributed to the study's conception and design. Material preparation, data collection, and analysis were performed by S Fakhri-Mirzanagh, G Pirgholi-Givi, and Y Azizian-Kalandaragh. The first draft of the manuscript was written by S Fakhri-Mirzanagh and S H R Shojaei, also, all authors commented on previous versions of the manuscript. All authors read and approved the final manuscript.

Funding

Data availability

The data will be made available on reasonable request.

Declarations

Competing interest   The authors promulgate that they have no known competing financial profits or personal relationships that could have appeared to affect the results reported in this manuscript.

Consent to participate   The authors declare their consent for publication.

References

1. S. Dong, J. Feng, M. Fan, Y. Pi, L. Hu, X. Han, J. Sun, RSC Adv. **5**(19), 14610 (2015). https://doi.org/10.1039/C4RA13734E

2. B.M. Al-Sakkaf, S. Nasreen, N. Ejaz, J. Chem. (2020). https://doi.org/10.1155/2020/8965627

3. X. Qu, J. Brame, Q. Li, P.J. Alvarez, Acc. Chem. Res. **46**(3), 834–843 (2013). https://doi.org/10.1021/ar300029v

4. N. Mukwevho, R. Gusain, E. Fosso-Kankeu, N. Kumar, F. Waanders, S.S. Ray, J. Ind. Eng. Chem. **81**, 393 (2020). https://doi.org/10.1016/j.jiec.2019.09.030

5. R. Gusain, N. Kumar, E. Fosso-Kankeu, S.S. Ray, ACS Omega **4**(9), 13922 (2019). https://doi.org/10.1021/acsomega.9b01603

6. R.K. Nath, M. Zain, A.A.H. Kadhum, J. Appl. Sci. Res. **8**(8), 4147 (2012)

7. H. Zhang, X. Lv, Y. Li, Y. Wang, J. Li, ACS Nano **4**, 380 (2010). https://doi.org/10.1021/nn901221k

8. N.B. Saber, A. Mezni, A. Alrooqi, T. Altalhi, J. Market. Res. **9**, 15233 (2020). https://doi.org/10.1016/j.jmrt.2020.10.090

9. D. Chatterjee, S. Dasgupta, J. Photochem. Photobiol. C **6**, 186 (2005). https://doi.org/10.1016/j.jphotochemrev.2005.09.001

10. M.R.D. Khaki, M.S. Shafeeyan, A.A.A. Raman, W.M.A.W. Daud, J. Environ. Manage. **198**, 78 (2017). https://doi.org/10.1016/j.jenvman.2017.04.099

11. M. Reza, A.S.W. Kurny, F. Gulshan, Appl Water Sci **7**, 1569 (2017)

12. M. Pirhashemi, A. Habibi-Yangjeh, S.R. Pouran, J. Ind. Eng. Chem. **62**, 1 (2018). https://doi.org/10.1016/j.jiec.2018.01.012

13. S. Fakhri-Mirzanagh, K. Ahadzadeh-Namin, G. Pirgholi-Givi, J. Farazin, Y. Azizian-Kalandaragh, Physica B **583**, 412064 (2020). https://doi.org/10.1016/j.physb.2020.412064

14. Y. Azizian-Kalandaragh, S. Fakhri-Mirzanagh, L. Badrinezhad, J. Nanoelectron. Optoelectron. **14**, 177 (2019). https://doi.org/10.1166/jno.2019.2467

15. M.M. Ali, M.A. Kudhier, R.S. Sabry, J. Phys. Conf. Series **1963**(1), 012119 (2021). https://doi.org/10.1088/1742-6596/1963/1/012119

16. Z. Ye, L. Kong, F. Chen, Z. Chen, Y. Lin, C. Liu, Optik **164**, 345 (2018). https://doi.org/10.1016/j.ijleo.2018.03.030

17. D. Wang, D. Li, L. Guo, F. Fu, Z. Zhang, Q. Wei, The J. Phys. Chem. C **113**(15), 5984–5990 (2009). https://doi.org/10.1021/jp810155r

18. O. Zelaya-Angel, R. Lozada-Morales, Phys. Rev. B **62**, 13064 (2000). https://doi.org/10.1103/PhysRevB.62.13064

19. F. Vaquero, R.M. Navarro, J.L.G. Fierro, Int. J. Hydrogen Energy **41**, 11558 (2016). https://doi.org/10.1016/j.ijhydene.2015.12.039

20. M. Milani, M. Mazzanti, G. Magnacca, S. Caramori, A. Molinari, Nanomaterials **13**, 413 (2023). https://doi.org/10.3390/nano13030413

21. P. Das, S. Saha, A.K. Bhunia, J. Mater. Sci. Mater. Electron. **35**(11), 763 (2024). https://doi.org/10.1007/s10854-024-12565-w

22. L. Gahramanli, M. Muradov, O. Balayeva, G. Eyvazova, J. Inorg. Organomet. Polym. Mater. **32**(9), 3395–3406 (2022). https://doi.org/10.1007/s10904-022-02458-y

23. L. Gahramanli, M. Muradov, Á. Kukovecz, O. Balayeva, G. Eyvazova, Inorg. Nano-Metal Chem. **50**(9), 808–815 (2020). https://doi.org/10.1080/24701556.2020.1725050

24. O.O. Balayeva, A.A. Azizov, M.B. Muradov, R.M. Alosmanov, G.M. Eyvazova, L.R. Gahramanli, M.A. Bayramov, J. Chin. Chem. Soc. **71**, 550 (2024). https://doi.org/10.1002/jccs.202300454

25. Z. Khan, M. Khannam, N. Vinothkumar, M. De, M. Qureshi, J. Mater. Chem. **22**(24), 12090–12095 (2012). https://doi.org/10.1039/C2JM31148H

26. Q. Li, B. Guo, J. Yu, J. Ran, B. Zhang, H. Yan, J.R. Gong, J. Am. Chem. Soc. **133**(28), 10878–10884 (2011). https://doi.org/10.1021/ja2025454

27. Y. Shi, X. Lei, L. Xia, Q. Wu, W. Yao, Chem. Eng. J. **393**, 124751 (2020). https://doi.org/10.1016/j.cej.2020.124751

28. Y. Chao, J. Zheng, J. Chen, Z. Wang, S. Jia, H. Zhang, Z. Zhu, Catal. Sci. Technol. **7**, 2798 (2017). https://doi.org/10.1039/C7CY00964J

29. C. Wang, J. Zhai, H. Jiang, D. Liu, L. Zhang, Solid State Sci. **98**, 106020 (2019). https://doi.org/10.1016/j.solidstatesciences.2019.106020

30. S.K. Maji, A.K. Dutta, D.N. Srivastava, P. Paul, A. Mondal, B. Adhikary, Polyhedron **30**(15), 2493–2498 (2011). https://doi.org/10.1016/j.poly.2011.06.029

31. N. Soltani, E. Saion, M.Z. Hussein, M. Erfani, A. Abedini, G. Bahmanrokh, P. Vaziri, Int. J. Mol. Sci. **13**, 12242 (2012). https://doi.org/10.3390/ijms131012242

32. D. Kim, S.H. Choi, C.O. Park, O. Byungsung, J. Mater. Sci. Mater. Electron. **9**, 31–34 (1998). https://doi.org/10.1023/A:1017338817011

33. M. Iqbal, A. Ibrar, A. Ali, F. Rehman, A.H. Jatoi, W.B. Jatoi, K.H. Thebo, Env. Technol. **43**, 1783 (2022). https://doi.org/10.1080/09593330.2020.1850880

34. K. Zhang, L. Jin, Y. Yang, K. Guo, F. Hu, J. Photochem. Photobiol., A **380**, 111859 (2019). https://doi.org/10.1016/j.jphotochem.2019.111859

35. D.V. Markovskaya, A.V. Zhurenok, S.V. Cherepanova, E.A. Kozlova, Appl. Surf. Sci. Adv. **4**, 100076 (2021). https://doi.org/10.1016/j.apsadv.2021.100076

36. L. Gahramanli, M. Muradov, A. Kukovecz, O. Balayeva, G. Eyvazova, S. Nuriyeva, J. Non-Oxide Glasses **11**(4), 57–63 (2019)

37. H. Zhang, Q. Feng, Y. Zhang, J. Zhang, X. Wu, Y. Li, X. Kong, Inorg. Chem. Front. **9**, 1100 (2022). https://doi.org/10.1039/D1QI01632F

38. C. Lu, S. Du, Y. Zhao, Q. Wang, K. Ren, C. Li, W. Dou, RSC Adv. **11**, 28211 (2021). https://doi.org/10.1039/D1RA04823F

39. G. Pirgholi-Givi, S. Farjami-Shayesteh, Y. Azizian-Kalandaragh, Physica B **575**, 311572 (2019). https://doi.org/10.1016/j.physb.2019.07.007

40. Y.T. Prabhu, K.V. Rao, V.S.S. Kumar, B.S. Kumari, World J. Nano Sci. Eng. **4**, 21–28 (2014). https://doi.org/10.4236/wjnse.2014.41004

41. Y.N. Xu, W.Y. Ching, Phys. Rev. B **48**, 4335 (1993). https://doi.org/10.1103/PhysRevB.48.4335

42. A.J. Frueh, Zeitschrift, für Kristallographie-Crystalline Materials **110**, 136 (1958). https://doi.org/10.1524/zkri.1958.110.16.136

43. D. Xu, R. Jiao, Y. Sun, D. Sun, X. Zhang, S. Zeng, Y. Di, Nanoscale Res. Lett. **11**, 1 (2016). https://doi.org/10.1186/s11671-016-1664-6

44. R. Sivakumar, C. Sanjeeviraja, J. Mater. Sci. Mater. Electron. **26**, 3670 (2015). https://doi.org/10.1007/s10854-015-2885-7

45. A.M. Alanazi, P.D. McNaughter, F. Alam, I.J. Vitorica-Yrezabal, G.F. Whitehea, F. Tuna, D. Lewis J, ACS Omega **6**, 27716 (2021). https://doi.org/10.1021/acsomega.1c02907

46. C.Y. Yeh, Z.W. Lu, S. Froyen, A. Zunger, Phys. Rev. B **46**, 10086 (1992). https://doi.org/10.1103/PhysRevB.46.10086

47. J. Kiwi, V. Nadtochenko, J. Phys. Chem. B **108**, 17675 (2004). https://doi.org/10.1021/jp048281a

48. E. Soto Morillo, N. Mota Toledo, J.L. García Fierro, R.M. Navarro Yerga, Hydrogen. **1**, 64 (2020). https://doi.org/10.3390/hydrogen1010005

49. L.W. Liu, S.Y. Hu, Y. Pan, J.Q. Zhang, Y.S. Feng, X.H. Zhang, Beilstein J. Nanotechnol. **5**, 919 (2014). https://doi.org/10.3762/bjnano.5.105

50. N. Phasook, S. Kamoldirok, W. Yindeesuk, J. Phys.: Conf. Series. **1144**(1), 012009 (2018). https://doi.org/10.1016/j.matpr.2023.07.018

51. W. Choi, J.Y. Choi, H. Song, APL Mater. (2019). https://doi.org/10.1063/1.5099666

52. Ghosh, S. (Ed.). Visible-light-active photocatalysis: nanostructured catalyst design, mechanisms, and applications. John Wiley & Sons. (2018).

53. E.L. Lyngdoh, V. Nayan, M. Vashisht, S. Kumari, A. Bhardwaj, T. Bhatia, D. Singh, Biotechnol. Lett. **42**, 1383 (2020). https://doi.org/10.1007/s10529-020-02896-z

54. L. Liu, K.T. Yong, I. Roy, W.C. Law, L. Ye, J. Liu, P.N. Prasad, Theranostics **2**, 705 (2012). https://doi.org/10.7150/thno.3456

55. A. Fatemi, M. Rasouli, M. Ghoranneviss, D. Dorranian, K.K. Ostrikov, Optical Mater. Express **12**, 2697 (2022). https://doi.org/10.1364/OME.456721

56. M. Kiani, M. Bagherzadeh, R. Kaveh, N. Rabiee, Y. Fatahi, R. Dinarvand, R.S. Varma, Nanomaterials **10**, 2320 (2020). https://doi.org/10.3390/nano10112320

57. A. Kudo, Pure Appl. Chem. **79**, 1917 (2007). https://doi.org/10.1351/pac200779111917

58. S.V. Kahane, R. Sasikala, B. Vishwanadh, V. Sudarsan, S. Mahamuni, Int. J. Hydrogen Energy **38**, 15012 (2013). https://doi.org/10.1016/j.ijhydene.2013.09.077

59. M.M. Rani, U. Shanker, Nanotechnol. Env. Eng. **8**, 197 (2023). https://doi.org/10.1007/s41204-022-00283-9

60. G. Ahmad, Y. Javed, Y. Jamil, K. Jilani, J. Mater. Sci. Mater. Electron. **33**, 12295 (2022). https://doi.org/10.1007/s10854-022-08188-8

61. A.R. Gandhe, J.B. Fernandes, J. Solid State Chem. **178**, 2953 (2005). https://doi.org/10.1016/j.jssc.2005.06.034

62. J.K. Reddy, K. Lalitha, P.V.L. Reddy, G. Sadanandam, M. Subrahmanyam, V.D. Kumari, Catal. Lett. **144**, 340 (2014). https://doi.org/10.1007/s10562-013-1112-5

63. R.H. Waghchaure, P.B. Koli, V.A. Adole, B.S. Jagdale, Results Chem. **4**, 100488 (2022). https://doi.org/10.1016/j.rechem.2022.100488

64. M.M. Sajid, S.B. Khan, N.A. Shad, N. Amin, Z. Zhang, RSC Adv. **8**, 23489 (2018). https://doi.org/10.1039/C8RA03890B

65. I.M. Ramírez-Sánchez, E.R. Bandala, Catalysts **8**, 625 (2018). https://doi.org/10.3390/catal8120625

66. Y. Matsumoto, M. Omae, I. Watanabe, E.I. Sato, J. Electrochem. Soc. **133**, 711 (1986). https://doi.org/10.1149/1.2108660

67. W. Guo, W.D. Chemelewski, O. Mabayoje, P. Xiao, Y. Zhang, C.B. Mullins, The J. Phys. Chem. C **119**, 27220 (2015). https://doi.org/10.1021/acs.jpcc.5b07219

68. H. Pan, S. Zhu, X. Lou, L. Mao, J. Lin, F. Tian, D. Zhang, RSC Adv. **5**, 6543 (2015). https://doi.org/10.1039/C4RA09546D

69. B. Zhang, S. Fu, D. Wang, S. Jiao, Z. Zeng, X. Zhang, J. Wang, Nanomaterials **11**, 2940 (2021). https://doi.org/10.3390/nano11112940

70. X. Liu, L. Pan, T. Lv, T. Lu, G. Zhu, Z. Sun, C. Sun, Catal. Sci. Technol. **1**, 1189 (2011). https://doi.org/10.1039/C1CY00109D

71. A.M. Tayeb, D.S. Hussein, Am. J. Nanomater. **3**, 57 (2015). https://doi.org/10.12691/ajn-3-2-2

72. L.R. Gahramanli, M.B. Muradov, J. Kim, G.M. Eyvazova, E.K. Gasimov, F.H. Rzayev, S. Bellucci, J. Mater. Sci. Mater. Electron. **35**(27), 1799 (2024). https://doi.org/10.1007/s10854-024-13539-8

73. F. Yang, N.N. Yan, S. Huang, Q. Sun, L.Z. Zhang, Y. Yu, The J. Phys. Chem. C **116**, 9078 (2012). https://doi.org/10.1021/jp300939q

74. I. Matsuura, M. Imaizumi, M. Sugiyama, Chem. Pharm. Bull. **38**, 1692 (1990). https://doi.org/10.1248/cpb.38.1692

75. K. Sorathiya, B. Mishra, A. Kalarikkal, K.P. Reddy, C.S. Gopinath, D. Khushalani, Sci. Rep. **6**, 35075 (2016). https://doi.org/10.1038/srep35075

76. H.E. Emam, H.B. Ahmed, E. Gomaa, M.H. Helal, R.M. Abdelhameed, Cellulose **27**, 7139 (2020). https://doi.org/10.1007/s10570-020-03282-8